Nanoscale

COMMUNICATION

View Article Online
View Journal

Cite this: DOI: 10.1039/c8nr08879a

Received 3rd November 2018,
Accepted 2nd December 2018

DOI: 10.1039/c8nr08879a

rsc.li/nanoscale

Tuning the oxygen evolution reaction on a nickel–iron alloy *via* active straining†

Anqi Wang,‡[a] Zhonglong Zhao,‡[b] Di Hu,[a] Junfeng Niu,[c] Man Zhang,[a] Kai Yan *[a] and Gang Lu*[b]

We report that one can gain active control of the electrocatalytic oxygen evolution reaction (OER) on Ni_3Fe thin films *via* externally applied strains. The combination of theory and experiments shows that an elastic strain on the surface can tune the OER activity in a predictable way that is consistent with the d-band model. The OER overpotential can be lowered by uniaxial tensions and increased by compressions in a linear manner.

Introduction

The role of surface strain in tuning electrocatalytic reactions has attracted significant interest recently.[1,2] The elastic strain can change the lattice spacing and/or the atomic structure on a catalyst surface. As a result, it can modify the surface chemistry of the catalyst, alter the reaction pathways and modulate the catalytic activities.[3–5] Both theory and experiments have demonstrated that by tuning the elastic strains on a catalyst surface, one can optimize its catalytic activity[3,6–8] whose enhancement is attributed to the shifts in the d-band center relative to the Fermi energy of the metal catalyst.[9–12]

The elastic strains can be applied to a metal surface either actively or passively. Previous research efforts have largely focused on passive straining of metal surfaces, for example, *via* core/shell nanostructures.[13–16] Due to the mismatch of the core/shell lattice parameters, elastic strains can be generated in the shells which in turn can boost catalytic reactions, such as the hydrogen evolution reaction (HER)[17–20] and the oxygen reduction reaction (ORR).[14,21–23] Despite its appeal, the effectiveness of passive straining depends crucially on the lattice misfit of the core/shell materials. For a given pair of core/shell materials, the surface strain is fixed in both magnitude and sign. As a result, one cannot tune the surface strain befitting for the reaction. Active straining, on the other hand, could circumvent this limitation by applying desirable strains directly to the materials *via* external loading. One can apply tension, compression or even oscillations between them to any material as long as the material can sustain the load, thus gaining active control of surface strains. Another advantage of active straining is the ability to directly study the strain effect on the activity, which is often intertwined in core/shell structures.[2,13] However, generating sufficient elastic strains on metal surfaces is highly challenging because most metals would deform plastically to relax the elastic strains on their surfaces. Nonetheless, progress has been made in active straining of catalysts. For instance, a small oscillatory tensile load was applied on Au and Pt to achieve a dynamic coupling between the strain and the ORR activity.[8,24] Our previous studies have shown that compressive strains applied on Pt, Ni, and WC and tensile strains on Cu could enhance the HER activity.[25,26] Active straining has also been demonstrated on Pd-based metallic glasses, NiTi shape memory alloys, and Pt films,[20–24] where compressive strains generally promoted the ORR activity while tensile strains impede the activity. To date, the greatest enhanced activity has been accomplished by 0.7% tensile strain, yielding ~15 mV reduction in the overpotential of the ORR.[8,24,27] Among these studies, noble-metal catalysts are the most widely utilized.

Inspired by these studies, we set out to expand the range of catalytic reactions that are responsive to active straining to the oxygen evolution reaction (OER) on noble-metal-free catalysts. In recent years, electrochemical water splitting has attracted significant interest as a key step for the production of clean

[a]*Guangdong Provincial Key Laboratory of Environmental Pollution and Remediation Technology, School of Environmental Science and Engineering, Sun Yat-sen University, 135 Xingang Xi Road, Guangzhou, 510275, China. E-mail: yank9@mail.sysu.edu.cn*

[b]*Department of Physics and Astronomy, California State University Northridge, Northridge, CA 91330, USA. E-mail: ganglu@csun.edu*

[c]*Research Center for Eco-Environmental Engineering, Dongguan University of Technology, Dongguan 523808, China*

†Electronic supplementary information (ESI) available: Computational methodology; XRD patterns and the valence band of Ni_3Fe thin films; the design and experimental setup; AFM measurements and SEM images of the Ni_3Fe thin films. See DOI: 10.1039/c8nr08879a

‡These authors contributed equally.

hydrogen from renewable sources such as solar, hydro, and wind.[28] Two reactions are involved – the HER from proton reduction and the OER from water oxidation.[29] Consisting of four-electron-transfer processes, the OER suffers from substantial overpotentials and energy loss at anodes,[30] baffling both theorists and experimentalists alike. Moreover, the state-of-the-art OER catalysts are generally composed of noble metals, such as Ir and Ru.[31] To the best of our knowledge, there is little effort or success in tuning OER activity on nonprecious metal catalysts *via* active straining. In this work, we examine the effect of active straining on the OER activity of nonprecious Ni_3Fe films fabricated on PMMA substrates with combined experimental and computational studies. The metal alloy films are subjected to externally applied uniaxial compressive and tensile strains to tune the OER *in situ*. In addition, we perform density functional theory (DFT) calculations to elucidate the physical origin of the enhanced OER activity and to interpret the experimental results.

Results and discussion

To ascertain the successful synthesis of the metal films, XRD and XPS were performed to characterize the crystal structures. As shown in Fig. S1,† the XRD pattern confirms the formation of an intermetallic Ni_3Fe alloy with anticipated crystalline orientations. Fig. S2† shows the valence band change between Ni, Fe and Ni_3Fe films. In the case of Ni_3Fe, the characteristic combination of Ni and Fe films can be clearly seen. The inductively coupled plasma optical emission spectrometer energy (ICP-OES) analysis shows the Ni/Fe molar ratio of 2.93, which is close to the stoichiometric ratio of 3. To investigate the effect of externally applied strains on the OER, Ni_3Fe films deposited on PMMA substrates are assembled into an electrochemical cell (Fig. S3†), and subsequently 100 initial CV scans at a sweep rate of 30 mV s^{-1} are performed to reach the steady state. In our initial experimental runs, the formation of shear bands was observed on the surface once the applied strain exceeded 0.5%. To avoid the onset of plastic deformation, we set the highest loading as 0.4% in the following experiments. The cycle of loading and unloading is depicted in Fig. 1a. During the electrocatalytic OER process, five cycles of CV scans are collected at each strain (0%, ±0.2% and ±0.4%). Fig. 1b shows a clear trend of the CVs collected at the tensile loading values (0%, 0.2% and 0.4%) during the oxygen evolution potential sweep. A systematic shift of the CV curve toward the applied strains is produced: tensile loading shifted the CV curves to the left (higher current density and lower overpotential), thus increasing the catalytic activity. Compressive strains display the opposite direction (Fig. 1c), *i.e.*, shifted the curves to the right, thus lowering the activity.

The voltage shifts induced by the strains are shown in Fig. 1d with error bars on each data point. We find that the voltage changes are approximately linear with the applied strains. The magnitude of the slope is over 18 mV per 1% strain, which is higher than what was achieved previously for

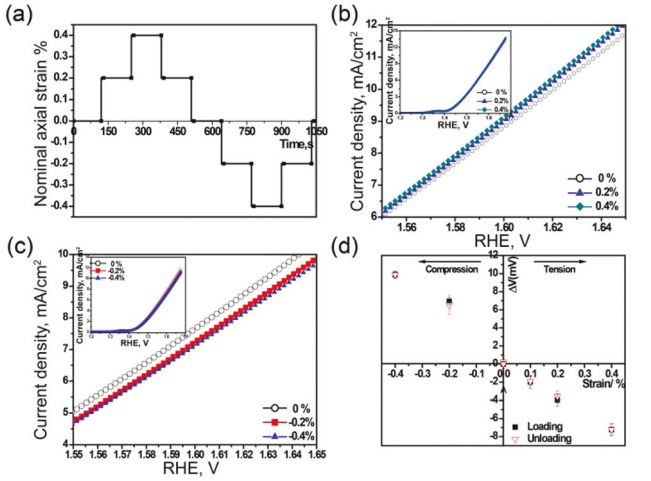

Fig. 1 (a) Schematic illustration of the loading history on the PMMA substrates. The Ni_3Fe films deposited on PMMA inherit the substrate strains. (b) Representative CVs obtained at tensile strains of 0%, 0.2% and 0.4%. (c) Representative CVs obtained at compressive strains of 0%, −0.2% and −0.4%. Note the systematic shift in the CV curves with strain. (d) Voltage change was calculated from CV curve shifts relative to the zero strain level *versus* the actively applied strain.

the HER (15 mV) and the ORR (16 mV).[25,27] The tensile strains are shown to enhance the OER activity, and 0.4% tensile strain leads to a reduction of overpotential by 7.3 mV.

DFT calculations are performed to elucidate the physical origin of the enhanced OER activity and to interpret the experimental data. Similar to previous studies,[32,33] we consider the following four-step OER reaction involving three intermediates (*OH, *O, and *OOH):

$$\begin{aligned} &H_2O + * \leftrightarrow *OH + H^+ + e^- \\ &\Delta G_1 = \Delta G_{*OH} - \Delta G_{H_2O} - eU + kT\ln[H^+] \end{aligned} \quad (1)$$

$$\begin{aligned} &*OH \leftrightarrow *O + H^+ + e^- \\ &\Delta G_2 = \Delta G_{*O} - \Delta G_{*OH} - eU + kT\ln[H^+] \end{aligned} \quad (2)$$

$$\begin{aligned} &*O + H_2O \leftrightarrow *OOH + H^+ + e^- \\ &\Delta G_3 = \Delta G_{*OOH} - \Delta G_{*O} - eU + kT\ln[H^+] \end{aligned} \quad (3)$$

$$\begin{aligned} &*OOH \leftrightarrow * + O_2 + H^+ + e^- \\ &\Delta G_4 = \Delta G_{O_2} - \Delta G_{*OOH} - eU + kT\ln[H^+]. \end{aligned} \quad (4)$$

The free energy change in each step (ΔG_1, ΔG_2, ΔG_3, and ΔG_4) defined in eqn (1)–(4) can be estimated by using the well-known Computational Hydrogen Electrode (CHE) model.[32–34] In this model, the free energy of an electron–proton pair is calculated as a half of the free energy for a hydrogen molecule ($1/2G_{H_2}$). The free energy of H_2O (ΔG_{H_2O}) and O_2 (ΔG_{O_2}) is taken as zero and 4.92 eV, respectively.[32,33] The overpotential, η, is defined as the minimal applied voltage U under which all four reaction steps are exothermic. In other words, $\eta = \max(\Delta G_1, \Delta G_2, \Delta G_3, \Delta G_4)/e$. For an optimal OER catalyst, it requires $\Delta G_1 = \Delta G_2 = \Delta G_3 = \Delta G_4$, resulting in a minimal η whose value is $\eta_{optimal} = (4.92–0)/4 = 1.23$ V. Practical OER catalysts have

overpotentials greater than $\eta_{optimal}$. In our calculations, the standard conditions such as pH = 0 and T = 298.15 K are assumed. More details about the CHE free energy calculations can be found elsewhere.[32,33]

Fig. 2a shows the OER free energy diagrams on the optimal OER catalyst (black), the clean Ni_3Fe (111) surface (grey), and the oxygen-covered Ni_3Fe (111) surface (blue) at a zero applied potential (U = 0 V). On the clean Ni_3Fe surface, we find that the reaction intermediates, *OH, *O, and *OOH, over-bind (with more negative free energies) on the surface as compared to the optimal catalyst, resulting in an overpotential of 4.77 V *vs.* RHE, which is much higher than the experimental onset potential (~1.4 V as shown in Fig. 1). Moreover, we find that the *OOH intermediate cannot be stabilized on the clean (111) surface. These results suggest that the OER is highly inefficient on the clean Ni_3Fe (111) surface. On the other hand, the adsorption of the OER intermediates can be drastically weakened on the oxygen-covered Ni_3Fe (111) surface, which in turn renders a significantly lowered overpotential of 2.03 V, much closer to the experimental onset potential. Therefore, we believe that under the experimental conditions, the (111) surface is covered by oxygen. To further examine the effect of oxygen coverage on the OER, we also calculate the free energy diagrams on partially oxygen-covered (111) surfaces by removing either one or three oxygen atoms adjacent to each reaction site. In the first case, we find that the free energy of *OH is lowered by only 0.09 eV compared to the full oxygen coverage, yielding a similar overpotential to that in the full coverage. However, if three oxygen atoms are removed, the free energy of *OH is reduced by 1.73 eV, rendering the partially oxygen-covered surface similar to the clean one with over-binding *OH species and a much higher overpotential. Therefore, we conclude that most metal sites on the Ni_3Fe (111) surface should be occupied by oxygen for a facile OER. Finally, since the free energy change in step 1 (ΔG_1) is greater than that in other three steps, step 1 ($H_2O + * \rightarrow *OH + H^+ + e^-$) is the overpotential-determining step on the oxygen-covered Ni_3Fe surface.

To examine the strain effect, we apply uniaxial tensile strains (0.2%, 0.4%, 0.6%, and 0.8%) to the oxygen-covered Ni_3Fe (111) surface. Fig. 2b shows the theoretical overpotential as a function of the applied strain. There is a monotonic correlation between the overpotential and the tensile strain; the larger the tension, the lower the overpotential, which is consistent with the experimental observation. For a uniaxial tensile strain of 0.4%, we predict that the OER overpotential is reduced by ~30 mV, which is larger than the corresponding experimental value of 7.3 mV. The smaller strain effect achieved in the experiments may be attributed to the possible strain relaxation on the surface and solution impedance in the experimental measurements.

To gain more insight into the strain effect, we calculate the shift of the d-band center on the oxygen-covered Ni_3Fe (111) surface under uniaxial tensile strains (Fig. 3). First of all, we note that the binding of the OER intermediates (such as *OH) on the oxygen-covered surface is weaker compared to the optimal catalyst (Fig. 2a). Thus, in order to enhance the OER activity, one needs to increase the binding of the intermediates. The calculated density of states for the d-band on the oxygen-covered surface in the absence and presence of 0.4%

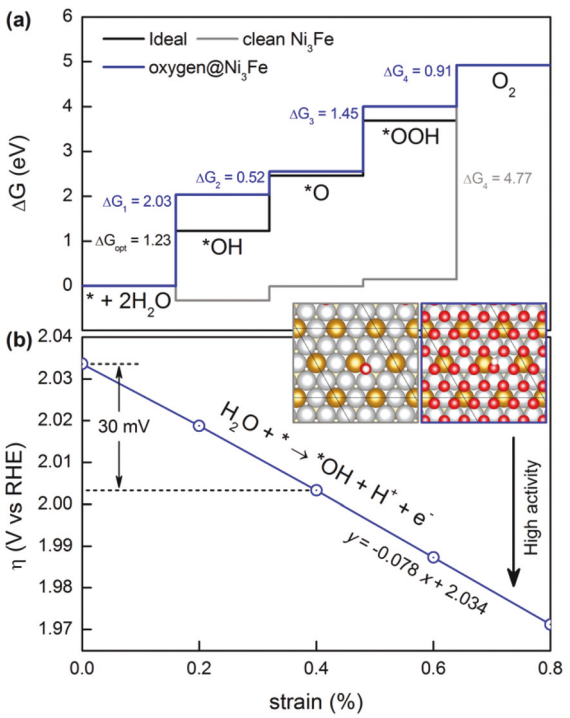

Fig. 2 (a) The OER free energy diagram for the optimal OER catalyst (black), clean Ni_3Fe (111) surface (grey), and oxygen-covered surface (blue) at a zero applied potential (U = 0 V *vs.* RHE). (b) The overpotential as a function of uniaxial tensile strain on the oxygen-covered Ni_3Fe surface. The top views of *OH adsorption on the clean and oxygen-covered (111) surfaces are shown in the insets. The gold, silver, red and white spheres represent Fe, Ni, O and H atoms, respectively.

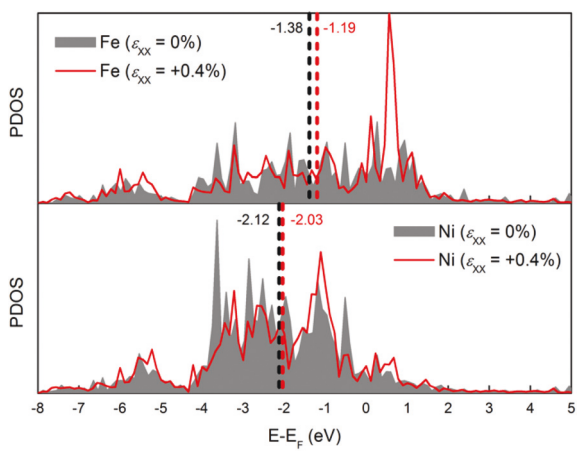

Fig. 3 The calculated density of states of the d-band (d_{z^2}) of the surface Fe atom (upper panel) and the Ni atom (lower panel) for the oxygen-covered Ni_3Fe (111) surface under zero and 0.4% tension. The vertical dashed lines indicate the d-band centers.

tensile strain is shown in Fig. 3. There is a clear upshift (towards the positive energy) of the d-band center for both surface Fe and Ni atoms under the tensile strain. This upshift of the d-band center is known to increase the binding of the intermediates,[35] thus enhancing the OER activity. Details about the DFT calculations are provided in the ESI.†

As a direct tool, atomic force microscopy (AFM) is used to investigate the surface roughness before and after the straining test. The roughness (R_a) of ~1.9 nm is measured in the as-prepared Ni_3Fe metal films (Fig. S4†), whereby the homogeneous surface is synthesized as confirmed by the surface roughness mapping. Scanning electron microscopy (SEM) images further show that there is no mechanical cracking or delamination on Ni_3Fe metal films during the strain test (Fig. S5†). Besides, the Ni_3Fe film after the straining and electrochemical tests exhibits the roughness R_a of ~2.7 nm (Fig. S6†), indicating that the physical surface area does not undergo detectable changes and the geometric current density is an appropriate measure.

Conclusions

In summary, by combining theory and experiments, we show that the externally applied strains can control the OER activity on Ni_3Fe films in a predictable manner. We reveal that the presence of oxygen on the Ni_3Fe (111) surface plays a crucial role in improving its OER activity. The observed strain-dependence of the OER activity can be explained by the d-band model. Theoretical calculations and experiments demonstrate that the uniaxial tensile strains can enhance the OER activity on Ni_3Fe films by lowering its overpotential. The tensile strain of 0.4% reduces the overpotential by 7.3 mV, which is the highest value reported on the strain effect in electrocatalysis. Our work represents the first effort in tuning OER activities on metallic alloys *via* active straining and provides a means to design noble-metal free catalysts for electrocatalysis.

Conflicts of interest

There are no conflicts to declare.

Acknowledgements

This work was supported by the National Key R&D Program of China (2018YFD0800700), the NSF PREM grant (DMR-1828019), the National Natural Science Foundation of China (21776324), the Science and Technology Planning Project of Guangdong Province, China (2014A050503032), the Guangdong Provincial Key Laboratory of Environmental Pollution Control and Remediation Technology (2018K02), and the Hundred Talent Plan (201602) from Sun Yat-sen University. The authors greatly acknowledge the previous help from Prof. A. Peterson and Prof. P. Guduru at Brown University.

References

1 M. Escudero-Escribano, P. Malacrida, M. H. Hansen, U. G. Vej-Hansen, A. Velazquez-Palenzuela, V. Tripkovic, J. Schiøtz, J. Rossmeisl, I. E. L. Stephens and I. Chorkendorff, *Science*, 2016, **352**, 73–76.
2 J. R. Kitchin, J. K. Nørskov, M. A. Barteau and J. G. Chen, *Phys. Rev. Lett.*, 2004, **93**, 156801.
3 R. Li, Y. Liu, H. Li, M. Zhang, Y. Lu, L. Zhang, J. Xiao, F. Boehm and K. Yan, *Small Methods*, 2018, DOI: 10.1002/smtd.201800344.
4 L. A. Kibler, A. M. El-Aziz, R. Hoyer and D. M. Kolb, *Angew. Chem., Int. Ed.*, 2005, **44**, 2080–2084.
5 R. Michalsky, Y. J. Zhang and A. A. Peterson, *ACS Catal.*, 2014, **4**, 1274–1278.
6 C. Cui, L. Gan, H. H. Li, S. H. Yu, M. Heggen and P. Strasser, *Nano Lett.*, 2012, **12**, 5885–5889.
7 J. Greeley, T. F. Jaramillo, J. Bonde, I. B. Chorkendorff and J. K. Norskov, *Nat. Mater.*, 2006, **5**, 909–913.
8 A. Khorshidi, J. Violet, J. Hashemi and A. A. Peterson, *Nat. Catal.*, 2018, **1**, 263–268.
9 Q. Deng, D. H. Gosslar, M. Smetanin and J. Weissmuller, *Phys. Chem. Chem. Phys.*, 2015, **17**, 11725–11731.
10 Q. Deng, M. Smetanin and J. Weissmüller, *J. Catal.*, 2014, **309**, 351–361.
11 V. A. Sethuraman, D. Vairavapandian, M. C. Lafouresse, T. A. Maark, N. Karan, S. Sun, U. Bertocci, A. A. Peterson, G. R. Stafford and P. R. Guduru, *J. Phys. Chem. C*, 2015, **119**, 19042–19052.
12 Y. Zheng, Y. Jiao, M. Jaroniec and S. Z. Qiao, *Angew. Chem., Int. Ed.*, 2015, **54**, 52–65.
13 M. C. Luo and S. J. Guo, *Nat. Rev. Mater.*, 2017, **2**, 17059.
14 S. Zhang, X. Zhang, G. Jiang, H. Zhu, S. Guo, D. Su, G. Lu and S. S. Sun, *J. Am. Chem. Soc.*, 2014, **136**, 7734–7739.
15 X. Zhang and G. Lu, *J. Phys. Chem. Lett.*, 2014, **5**, 292–297.
16 Z. Chen, X. Zhang and G. Lu, *J. Phys. Chem. C*, 2017, **121**, 1964–1973.
17 H. Wolfschmidt, R. Bussar and U. Stimming, *J. Phys.: Condens. Matter*, 2008, **20**, 374127.
18 D. Voiry, H. Yamaguchi, J. Li, R. Silva, D. C. B. Alves, T. Fujita, M. Chen, T. Asefa, V. B. Shenoy, G. Eda and M. Chhowalla, *Nat. Mater.*, 2013, **12**, 850–855.
19 T. Ling, D. Y. Yan, H. Wang, Y. Jiao, Z. Hu, Y. Zheng, L. Zheng, J. Mao, H. Liu, X. W. Du, M. Jaroniec and S. Z. Qiao, *Nat. Commun.*, 2017, **8**, 1509.
20 T. A. Maark and A. A. Peterson, *J. Phys. Chem. C*, 2014, **118**, 4275–4281.
21 C. Cui, M. Ahmadi, F. Behafarid, L. Gan, M. Neumann, M. Heggen, B. Roldan Cuenya and P. Strasser, *Faraday Discuss.*, 2013, **162**, 91–112.
22 P. Strasser, S. Koh, T. Anniyev, J. Greeley, K. More, C. Yu, Z. Liu, S. Kaya, D. Nordlund, H. Ogasawara, M. F. Toney and A. Nilsson, *Nat. Chem.*, 2010, **2**, 454–460.
23 L. Wang, A. Holewinski and C. Wang, *ACS Catal.*, 2018, **8**, 9388–9398.

24 M. Du, L. Cui, Y. Cao and A. J. Bard, *J. Am. Chem. Soc.*, 2015, **137**, 7397–7403.
25 K. Yan, T. A. Maark, A. Khorshidi, V. A. Sethuraman, A. A. Peterson and P. R. Guduru, *Angew. Chem., Int. Ed.*, 2016, **55**, 6175–6181.
26 K. Yan, S. K. Kim, A. Khorshidi, P. R. Guduru and A. A. Peterson, *J. Phys. Chem. C*, 2017, **121**, 6177–6183.
27 Y. Yang, T. A. Maark, A. Peterson and S. Kumar, *Phys. Chem. Chem. Phys.*, 2015, **17**, 1746–1754.
28 T. R. Cook, D. K. Dogutan, S. Y. Reece, Y. Surendranath, T. S. Teets and D. G. Nocera, *Chem. Rev.*, 2010, **110**, 6474–6502.
29 M. D. Symes and L. Cronin, *Nat. Chem.*, 2013, **5**, 403–409.
30 K. Yan and Y. Lu, *Small*, 2016, **22**, 2975–2981.
31 C. C. L. McCrory, S. H. Jung, J. C. Peters and T. F. Jaramillo, *J. Am. Chem. Soc.*, 2013, **135**, 16977–16987.
32 S. Wannakao, T. Maihom, K. Kongpatpanich, J. Limtrakul and V. Promarak, *Phys. Chem. Chem. Phys.*, 2017, **19**, 29540–29548.
33 I. C. Man, H. Y. Su, F. Calle-Vallejo, H. A. Hansen, J. I. Martínez, N. G. Inoglu, J. Kitchin, T. F. Jaramillo, J. K. Nørskov and J. Rossmeisl, *ChemCatChem*, 2011, **3**, 1159–1165.
34 J. K. Nørskov, J. Rossmeisl, A. Logadottir, L. Lindqvist, J. R. Kitchin, T. Bligaard and H. Jónsson, *J. Phys. Chem. B*, 2004, **108**, 17886–17892.
35 A. Ruban, B. Hammer, P. Stoltze, H. L. Skriver and J. K. Nørskov, *J. Mol. Catal. A: Chem.*, 1997, **115**, 421–429.